




Fractional-Order Complementary Terminal Sliding Mode Control of Active Power Filter Based on Improved Reptile Search Algorithm

Guangrun Yang¹, Zhichuan Li², Tengbin Li³, Junchao Chang^{4*} 

^{1, 2, 3, 4} Measurement Center of Yunnan Power Grid Co. Ltd., Kunming, China

E-mail: cky_ben@163.com

Received: 18 Dec, 2024

Revised: 18 Apr, 2025

Accepted: 24 Apr, 2025

Available online: May 22, 2025

Abstract— This paper proposes an enhanced fractional-order complementary terminal sliding mode (FOCTSM) control strategy for active power filter (APF), incorporating an improved reptile search algorithm (IRSA) with reverse learning strategy and the Cauchy mutation. The proposed method leverages the inherent advantages of fractional-order control, including superior design flexibility and precision, to address the critical requirements of harmonic suppression and current tracking in APF applications. Firstly, a FOCTSM surface is designed based on current error, followed by the development of a new exponential sliding mode reaching law. Secondly, IRSA is employed to optimize the fractional-order parameters and control gains. Finally, the simulation model of the APF is built by the SIMULINK toolbox, and the simulation verification and analysis comparison are conducted. The simulation results reveal that the current total harmonic distortion (THD) is reduced from 25.41% to 0.67% after filtering. Moreover, under disturbances, the current tracking absolute error remains below 0.2. These results demonstrate that the proposed optimal control strategy improves both harmonic suppression and robustness in the APF system.

Keywords— Fractional-order complementary terminal sliding mode control; Improved reptile optimization algorithm; Current tracking; Active power filter.

1. INTRODUCTION

The increasing integration of renewable energy sources and nonlinear loads into distribution networks has led to a growing severity of harmonic pollution [1, 2]. As a crucial indicator for assessing power quality, harmonic analysis holds significant importance in both theoretical research and engineering applications. Among various mitigation approaches, the active power filter (APF) has been widely adopted as an effective solution for dynamic harmonic suppression [3].

In the APF, accurate current tracking control in the inner loop is crucial for achieving harmonic compensation [4]. Sliding mode control (SMC), a nonlinear control method known for its structural simplicity and strong robustness, has been extensively adopted in APF current-loop controller design [5]. However, conventional SMC suffers from chattering issues. To address this problem, various improved SMC strategies have been proposed, including fuzzy integral SMC [6], adaptive SMC [7], and complementary SMC (CSMC) [8]. Among these, CSMC combines the generalized SMC and CSMC, which can reduce the chattering amplitude and enhance the robustness of the system. In [8], authors employed the CSMC method for speed control in permanent-magnet synchronous motor (PMSM) drives, achieving a 50% reduction in tracking error compared to conventional SMC with saturation function.

* Corresponding author

Nevertheless, CSMC cannot guarantee a finite-time convergence of tracking errors to zero. To address this limitation, the authors in [9] developed a terminal sliding mode (TSM) control scheme that achieves simultaneous finite-time convergence of the sliding surface and tracking error. However, all sliding mode controllers presented in [6-9] utilize integer order calculus, potentially limiting controller flexibility and performance. Owing to the inherent advantages of fractional calculus, researchers have developed fractional-order sliding mode controllers that partially overcome these limitations. Yet determining optimal control parameters and fractional orders remains a significant challenge in control engineering. To deal with this, some researchers tried to introduce heuristic optimization algorithms to optimize the controller parameters. For instance, references [10] and [11] respectively applied the Cuckoo Search Algorithm and an improved Sparrow Search Algorithm to optimize fractional-order PID controllers, demonstrating enhanced system performance. Nevertheless, research on parameter for the fractional-order sliding mode control remains insufficient and requires further investigation. Based on the above analysis, to further enhance the filter effect and current tracking performance of the APF, and suppress system oscillations, this paper proposes a fractional-order complementary terminal sliding mode (FOCTSM) control based on an improved reptile search algorithm. Main contributions are listed as follows:

- a) A fractional-order complementary terminal sliding surface is proposed, extending integer-order approaches by introducing fractional-order degrees of freedom. This enables more precise error convergence. Additionally, a novel sliding mode reaching law is designed, demonstrating superior convergence speed and reduced chattering compared to existing methods.
- b) An improved reptile search algorithm is developed, incorporating reverse learning strategy and Cauchy mutation function for optimal parameter and order selection. This prevents premature convergence and enhances global search capability.
- c) Compared with TSMC and CSMC, the proposed strategy achieves significant THD reductions of 61.7% and 52.1%, respectively. Furthermore, the THD is reduced by 39.6% compared to pre-optimization and by 33.7% when compared with the conventional and improved RSA. The method maintains robust performance under disturbances, with current tracking errors consistently below 0.2 A. These results confirm that the proposed optimal control strategy simultaneously enhances both harmonic suppression and current tracking capabilities in APF applications.

2. MODEL DESCRIPTION

In this part, the circuit model for the APF is depicted in Fig. 1. According to Fig. 1 and Kirchhoff's theorem, the mathematical model of the circuit is obtained as follows:

$$\begin{cases} \frac{di_{ca}}{dt} = \frac{1}{L}(u_{va} - ri_{ca} + h_a U_{dc}) \\ \frac{di_{cb}}{dt} = \frac{1}{L}(u_{vb} - ri_{cb} + h_b U_{dc}) \\ \frac{di_{cc}}{dt} = \frac{1}{L}(u_{vc} - ri_{cc} + h_c U_{dc}) \end{cases} \quad (1)$$

where, u_{vk} ($k=a, b, c$) denotes the power voltage, U_{dc} denotes the DC-side voltage, i_{ck} denotes the compensation current, r denotes equivalent resistance on the AC side of the APF, L denotes the equivalent inductance of the APF AC-side, h_k denotes the control function.

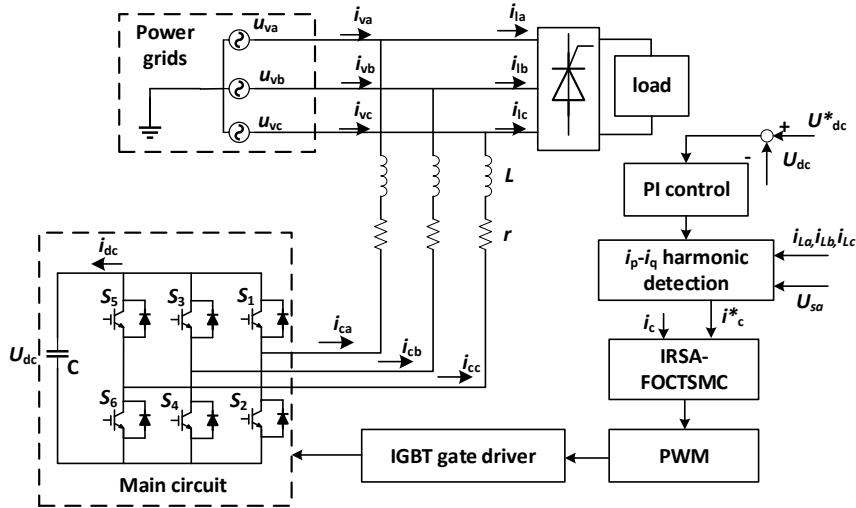


Fig. 1. Circuit model of the APF.

As shown in Fig. 1, the circuit model of the three-phase shunt APF primarily consists of the power grid, an inverter circuit, and a nonlinear load. In the inverter circuit, IGBTs serve as switching devices. The reference current i_c^* is obtained in real-time by decomposing grid voltage/current signals using the i_p-i_q detection algorithm based on instantaneous reactive power theory. The reference current i_c^* and compensation current i_c act as input signals for the IRSA-FOCTSM controller. The control algorithm processes these signals to generate the PWM input, which then drives the IGBTs' switching actions to produce the compensating current i_c . The DC-side capacitor functions to stabilize the DC voltage, preventing significant fluctuations caused by active power losses.

3. DESIGN OF THE CONTROLLER AND STABILITY ANALYSIS

In this part, the FOCTSM controller based on improved reptile search algorithm (IRSA) is designed and the stability of the APF with control is analyzed.

Definition [11]: The Caputo derivative of order m of the continuous function $f \in C^\alpha([0, t], R)$ is described as

$${}^c D_t^\alpha f(t) = \frac{1}{\Gamma(\alpha)} \int_0^t (t-\xi)^{\alpha-1} f(\xi) d\xi, \quad n-1 < \alpha < n \quad (2)$$

where t denotes the upper bound of the operator; α denotes the order; n is a positive integer; Γ denotes the Gamma function. For simplicity, the symbol D^α is used in place of ${}^c D_t^\alpha$ in the subsequent sections.

3.1. Design of the Controller

Reference [8] demonstrates that the complementary sliding mode surface can effectively reduce tracking error and enhance system performance. However, unlike terminal sliding mode, it cannot achieve finite-time convergence. To overcome this limitation, a terminal sliding mode surface is incorporated into the complementary sliding mode framework, resulting in a complementary terminal sliding mode surface (CTSMS). This hybrid approach combines the benefits of both methods. Additionally, fractional calculus further improves the design flexibility of CTSMS due to its inherent advantages. Thus, to enhance the harmonic control

performance of the APF, this study adopts fractional-order complementary terminal sliding mode control (FOCTSMC) as the current tracking control strategy.

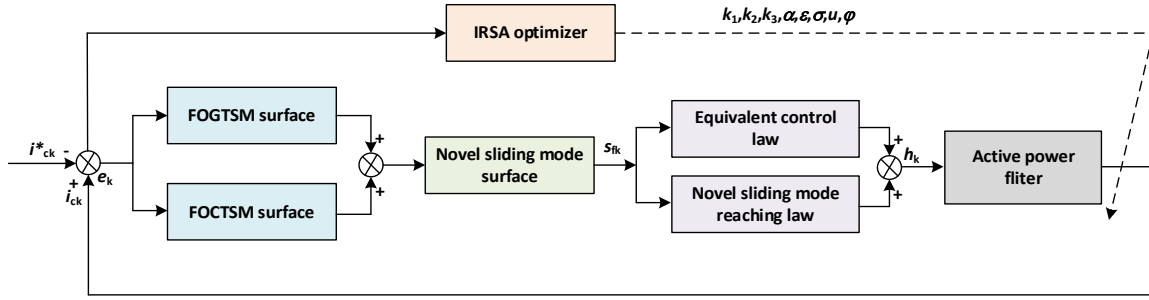


Fig. 2. Block diagram of the IRSA-FOCTSMC.

The proposed fractional-order complementary terminal sliding mode control (FOCTSMC) scheme is illustrated in Fig. 2. In this controller, the novel sliding mode surface consists of a fractional-order generalized terminal sliding mode (FOGTSM) surface and a fractional-order complementary terminal sliding mode (FOCTSM) surface. All controller parameters are optimized by the improved reptile search algorithm (IRSA). Considering the mathematical model of the APF circuit, we define the following:

First of all, to ensure that the compensating current closely matches the reference current, the error e_k between them is defined as:

$$e_k(t) = i_{ck}(t) - i_{ck}^*(t) \quad (3)$$

where $i_{ck}^*(t)$ denotes reference current, $i_{ck}(t)$ denotes compensation current, $k=a,b,c$.

Secondly, the FOGTSM surface $s_{fgk}(t)$ and the FOCTSM surface $s_{fck}(t)$ are designed as follows:

$$\begin{aligned} s_{fgk}(t) &= (D^\alpha + \varepsilon)^2 D^{-\alpha} e_k(t) + e_k^\delta(t) + \varepsilon D^{-\alpha} e_k^\delta(t) \\ &= D^\alpha e_k(t) + 2\varepsilon e_k(t) + \varepsilon^2 D^{-\alpha} e_k(t) \\ &\quad + e_k^\delta(t) + \varepsilon D^{-\alpha} e_k^\delta(t) \end{aligned} \quad (4)$$

$$\begin{aligned} s_{fck}(t) &= (D^\alpha + \varepsilon)(D^\alpha - \varepsilon) D^{-\alpha} e_k(t) + e_k^\delta(t) - \varepsilon D^{-\alpha} e_k^\delta(t) \\ &= D^\alpha e_k(t) - \varepsilon^2 D^{-\alpha} e_k(t) + e_k^\delta(t) - \varepsilon D^{-\alpha} e_k^\delta(t) \end{aligned} \quad (5)$$

where α denotes fractional-order; $\varepsilon > 0$ is a constant; δ is a positive constant between 0 and 1.

Then, the new sliding mode surface $s_{fk}(t)$ is given as:

$$\begin{aligned} s_{fk}(t) &= s_{fgk}(t) + s_{fck}(t) \\ &= 2D^\alpha e_k(t) + 2\varepsilon e_k(t) + 2e_k^\delta(t) \end{aligned} \quad (6)$$

Next, by differentiating $s_{fgk}(t)$ and $s_{fck}(t)$, the following expressions are obtained:

$$D^\alpha s_{fgk}(t) = D^{2\alpha} e_k(t) + 2\varepsilon D^\alpha e_k(t) + \varepsilon^2 e_k(t) + D^\alpha e_k^\delta(t) + \varepsilon e_k^\delta(t) \quad (7)$$

$$D^\alpha s_{fck}(t) = D^{2\alpha} e_k(t) - \varepsilon^2 e_k(t) + D^\alpha e_k^\delta(t) - \varepsilon e_k^\delta(t) \quad (8)$$

Therefore, combining Eqs. (7) and (8), the following equation can be achieved:

$$D^\alpha s_{fgk}(t) - D^\alpha s_{fck}(t) = \varepsilon s_{fk}(t) \quad (9)$$

Thirdly, by combining the continuous and smooth properties of the arcsinh and tanh functions with the rapid convergence characteristics of the exponential function, the following new sliding mode reaching law is designed as:

$$\dot{s}_{fk} = -k_1 s_{fk} \sqrt{s_{fk}^2 + 1} - k_2 |s_{fk}|^\varphi \operatorname{arsinh}(s_{fk}/\sigma) - k_3 \ln(|s_{fk}|^\nu + 1) \tanh(s_{fk}(t)) \quad (10)$$

where, k_1, k_2 and σ are positive constants, φ is a positive constant between 0 and 1, $k=a,b,c$.

Additionally, to verify the superiority of the proposed reaching law, a comparison is made with the traditional exponential reaching law RL1 ($\dot{s} = -k_4 s - k_5 \text{sign}(s)$), the double power reaching law RL2 ($\dot{s} = -k_6 |s|^\delta \text{sign}(s) - k_7 |s|^\varepsilon \text{sign}(s)$) from [12], and the reaching law RL3 ($\dot{s} = -k_8 s - k_9 \tanh(a_3 |s|) \text{sign}(s)$) proposed in [13].

Here, the typical system shown in Eq. (11) is used to conduct simulation verification of the sliding mode reaching law.

$$\frac{dx}{dt} = Fx + Ju \quad (11)$$

where, $x = [x_1 \ x_2]^T$, x_1 and x_2 denote state variables, $F = \begin{bmatrix} 1 & 0.001 \\ 0 & 0.9753 \end{bmatrix}$, $J = \begin{bmatrix} -0.001 \\ -0.1314 \end{bmatrix}$, u denotes control function of the system.

The parameter values for each reaching law, all of which are user-defined, are listed in Table 1.

Table 1. The Parameters for reaching Laws.

Parameter	Value	Parameter	Value	Parameter	Value
k_1	5000	k_6	5000	θ	1.05
k_2	500	k_7	1000	φ	1.05
k_3	500	k_8	5000	ε	100
k_4	5000	k_9	1000	σ	2
k_5	1000	δ	1	α	0.001

As illustrated in the Fig. 3, the proposed reaching law in this paper demonstrates a significantly faster convergence compared to other reaching laws. Additionally, as the system approaches the equilibrium point, the proposed reaching law enables the system to approach the sliding mode surface more quickly and smoothly. Therefore, it can be concluded that the designed reaching law has more advantages.

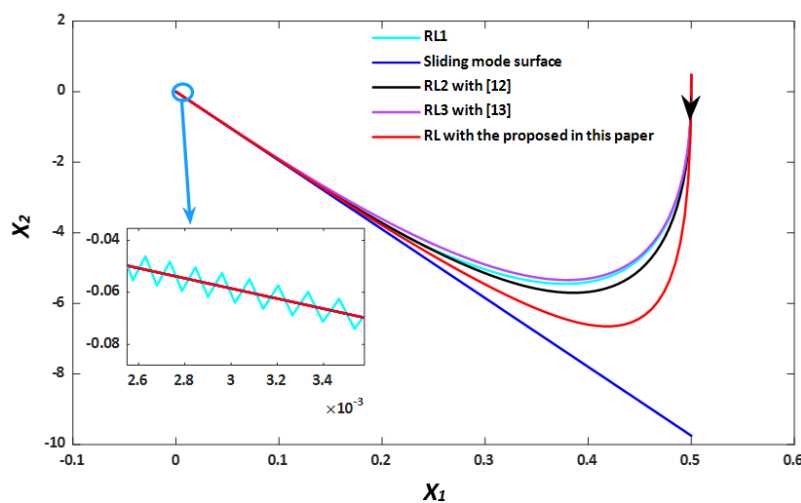


Fig. 3. Phase trajectory diagram of reaching sliding mode surface with different reaching laws.

Finally, choosing the Lyapunov function V as follow:

$$V = \frac{1}{2} (s_{fgk}^2 + s_{fck}^2) \quad (12)$$

and by differentiating V with respect to time t , the following expression is obtained:

$$D^\alpha V(t) \leq s_{fgk}(t) D^\alpha s_{fgk}(t) + s_{fck}(t) D^\alpha s_{fck}(t) \quad (13)$$

Then, substituting Eq. (9) into Eq. (13), and combining Eq. (6), it yields:

$$\begin{aligned} D^\alpha V(t) &\leq s_{fgk}(t) D^\alpha s_{fgk}(t) + s_{fck}(t) (D^\alpha s_{fgk}(t) - \varepsilon s_{fk}(t)) \\ &= s_{fgk}(t) D^\alpha s_{fgk}(t) + s_{fck}(t) D^\alpha s_{fgk}(t) - s_{fck}(t) \varepsilon s_{fk}(t) \\ &= (s_{fgk}(t) + s_{fck}(t)) D^\alpha s_{fgk}(t) - s_{fck}(t) \varepsilon s_{fk}(t) \\ &= s_{fk}(t) D^\alpha s_{fgk}(t) - s_{fk}(t) \varepsilon s_{fck}(t) \\ &= s_{fk}(t) (D^\alpha s_{fgk}(t) - \varepsilon s_{fck}(t)) \end{aligned} \quad (14)$$

Next, substituting Eqs. (1), (3), and (7) into Eq. (14), we have:

$$\begin{aligned} D^\alpha V(t) &\leq s_{fk}(t) (D^\alpha s_{fgk}(t) - \varepsilon s_{fck}(t)) \\ &= s_{fk} (D^{2\alpha} e_k(t) + 2\varepsilon D^\alpha e_k(t) + \varepsilon^2 e_k(t) + D^\alpha e_k^\delta(t) \\ &\quad + \varepsilon e_k^\delta(t) - \varepsilon s_{fck}(t)) \\ &= s_{fk} [D^{2\alpha-1} \dot{e}_k(t) + 2\varepsilon D^\alpha e_k(t) + \varepsilon^2 e_k(t) \\ &\quad + D^\alpha e_k^\delta(t) + \varepsilon e_k^\delta(t) - \varepsilon s_{fck}(t)] \\ &= s_{fk} \left[D^{2\alpha-1} \left(\frac{1}{L} (u_{vk} - r_{ck} + h_k u_{dc}) - i_{ck}^*(t) \right) \right. \\ &\quad \left. + 2\varepsilon D^\alpha e_k(t) + \varepsilon^2 e_k(t) + D^\alpha e_k^\delta(t) + \varepsilon e_k^\delta(t) - \varepsilon s_{fck}(t) \right] \end{aligned} \quad (15)$$

Let the Eq. (15) be equal to zero, thereby obtaining the equivalent control law h_{eqk} as follow:

$$\begin{aligned} h_{eqk} &= \frac{L}{U_{dc}} \left(i_{ck}^*(t) - \frac{u_{vk}}{L} + \frac{r_{ck}(t)}{L} + D^{1-2\alpha} \varepsilon s_{fck}(t) - 2\varepsilon D^{1-\alpha} e_k(t) \right. \\ &\quad \left. - D^{1-2\alpha} \varepsilon^2 e_k(t) - D^{1-\alpha} e_k^\delta(t) - D^{1-2\alpha} \varepsilon e_k^\delta(t) \right) \end{aligned} \quad (16)$$

Based on Eq. (10) and to ensure the designed controller satisfies Lyapunov's stability theorem, the reaching law for the APF is designed as follows:

$$\begin{aligned} h_{rlk} &= \frac{L}{u_{dc}} \left[-k_1 s_{fk} \sqrt{s_{fk} + 1} - k_2 |s_{fk}|^\rho \operatorname{asinh} \left(\frac{s_{fk}}{\sigma} \right) \right. \\ &\quad \left. - k_3 \ln(|s_{fk}|^\rho + 1) \tanh(s_{fk}(t)) \right] \end{aligned} \quad (17)$$

Thus, the FOCTSMC law designed is obtained as follow:

$$h_k = h_{eqk} + h_{rlk} \quad (18)$$

Remark: The designed sliding mode reaching law in this paper consists of three terms:

Term 1: $-k_1 s_{fk} \sqrt{s_{fk} + 1}$,

Term 2: $-k_2 |s_{fk}|^\rho \operatorname{asinh}(s_{fk}/\sigma)$,

Term 3: $-k_3 \ln(|s_{fk}|^\rho + 1) \tanh(s_k(t))$.

When the error is far from the sliding mode surface, Term 1 dominates for fast convergence. Once the error reaches the sliding mode surface and moves towards the equilibrium point, Term 2 combined with Term 3 primarily takes effect. Additionally, The

switching gain incorporates exponential-logarithmic $s(t)$ for adaptive coefficient adjustment, effectively reducing chattering.

3.2. Improved Reptile Search Algorithm

To optimize the parameters and fractional orders of the proposed control strategy for enhanced harmonic suppression performance in APF, this paper employs an improved reptile search algorithm (IRSA) for parameter tuning. The RSA simulates crocodiles' hunting behavior, consisting of two primary phases: exploration and exploitation. The exploration phase incorporates both high- and low-level searches to establish a suitable search space. Subsequently, the exploitation phase is subdivided into coordination and cooperation for identifying optimal solutions within the defined search space. For implementation details, refer to Reference [14].

Although the conventional RSA has demonstrated effectiveness in solving optimization problems, it suffers from inherent limitations including slow convergence rates and premature convergence to local optima. To overcome these drawbacks, this paper proposes the following enhancements:

- 1) Introduction of Reverse Learning Strategy: During the population initialization phase, to build an elite crocodile population and enhance the probability of discovering the optimal solution, the following reverse learning strategy is introduced:

$$P'_{i,j} = k(B_{u,j} + B_{l,j}) - P_{i,j} \quad (19)$$

$$P'_{i,j} = B_{u,j}, \quad P'_{i,j} > B_{u,j} \quad (20)$$

$$P'_{i,j} = B_{l,j}, \quad P'_{i,j} < B_{l,j} \quad (21)$$

where $P_{i,j}$ is the value of the i -th crocodile in the j -th dimension; $P'_{i,j}$ is the reverse solution of a regular crocodile; $B_{u,j}$ and $B_{l,j}$ are the upper and lower bounds for the j -th dimension, respectively; k is the elite reverse coefficient, which is a random number in the range (0, 1).

- 2) Introducing Cauchy mutation. To avoid the algorithm from becoming stuck in a local optimum, applying Cauchy mutation to the current best solution to achieve a global optimum. The Cauchy mutation process is as follow:

$$P_{nb} = P_b + P_b \cdot \text{Cauchy}(0,1) \quad (22)$$

where P_b denotes current optimal solution, P_{nb} denotes optimal solution after the Cauchy mutation, and $\text{Cauchy}(0,1)$ denotes Cauchy function.

Building upon prior research, this paper develops a fractional-order complementary terminal sliding mode controller (FOCTSMC) enhanced by an improved Reptile Search Algorithm (IRSA) to simultaneously improve compensating current tracking accuracy and filtering performance. As illustrated in Fig. 4, the proposed framework implements the following key procedures:

- ① Initialize: Set the number of crocodiles N , the maximum number of iterations T , and other parameters.
- ② Reverse Solutions: Obtain the reverse solutions of the population using Eqs. (19) to (21) and construct the elite crocodile population.
- ③ Fitness Calculation: Calculate the fitness values of the population individuals, obtain the current optimal solution, and apply Cauchy mutation to the current optimal solution using Eq. (22).
- ④ Update: Update the positions of individuals and related parameters.

- ⑤ Boundary Check: Check if the individual positions are within the bounds.
 ⑥ Iteration Check: Determine if the iteration is complete. If not, repeat steps ② to ⑤.

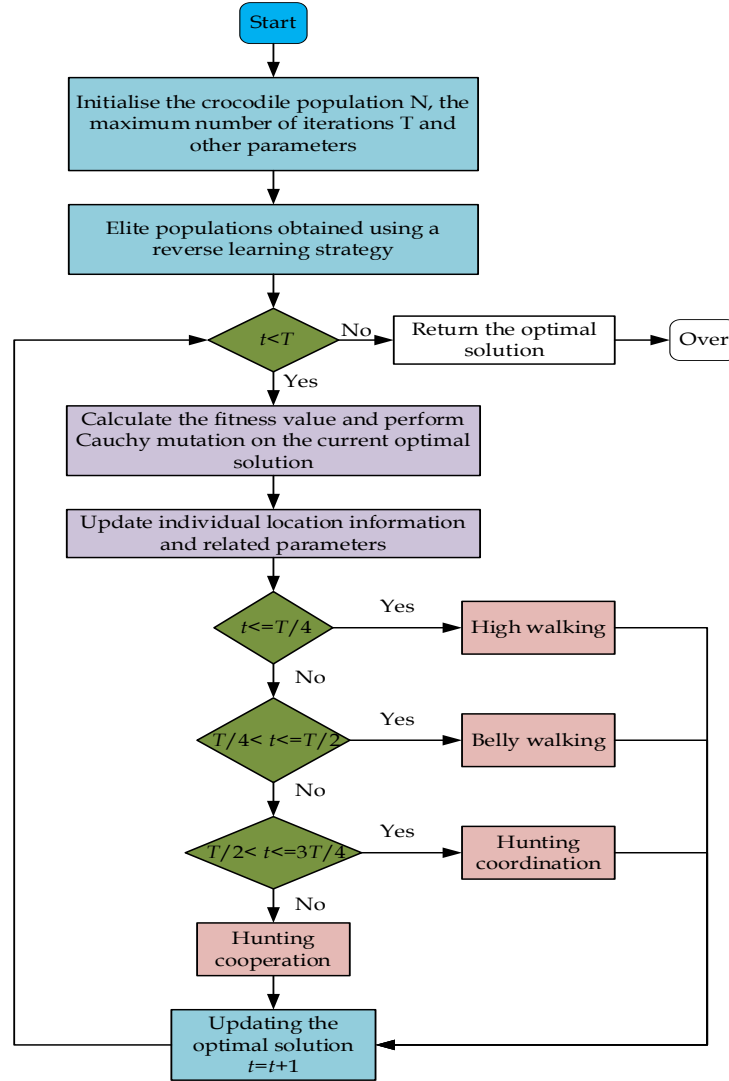


Fig. 4. Flowchart of the IRSA.

The standard test function (namely, Sphere function) is used to simulate the RSA before and after improvement. The expression for the Sphere function is shown in Eq. (23), and the comparison result is shown in Fig. 5.

$$f(x) = \min \sum_{i=1}^{50} x_i^2 \quad (23)$$

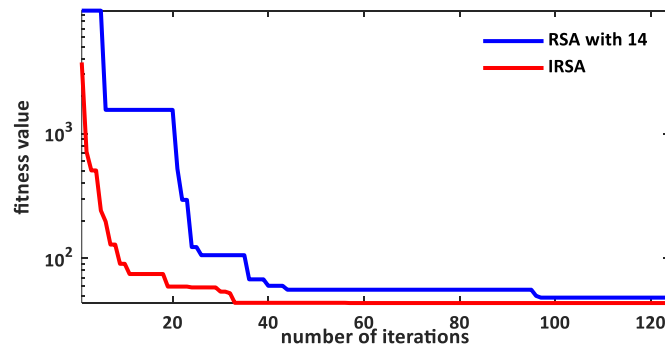


Fig. 5. Comparison results of the RSA and the IRSA.

From the Fig. 5, it can be observed that the convergence speed of the IRSA is significantly faster than that of the RSA, and the fitness value of the IRSA is lower than that of the RSA. This indicates that the IRSA has higher convergence accuracy and faster convergence speed.

Next, based on the IRSA, to optimize the control parameters and the order of the proposed controller, the following objective function is constructed:

$$\left\{ \begin{array}{l} \min f = \int_0^{\theta} |i_c(t) - i_c^*(t)| dt \\ \text{s.t.} \left\{ \begin{array}{l} 0 < \alpha < 1 \\ 0 < \nu < 2 \\ 0 < \varphi < 2 \\ 0 < k_1 < 1000 \\ 0 < k_2 < 1000 \\ 0 < k_3 < 1000 \\ 0 < \sigma < 1000 \\ 0 < \varepsilon < 10000 \end{array} \right. \end{array} \right. \quad (24)$$

where θ is the upper limit of the integration time. Additionally, the population size is set at 8, and the maximum number of iterations is set at 50.

4. ILLUSTRATIVE EXAMPLES

To verify the effectiveness and superiority of the proposed control strategy, the APF is built and simulated in SIMULINK toolbox of the MATLAB. The simulation parameters are shown in Table 2 [8]:

Table 2 APF simulation parameters.

System parameter	Value
AC Power	$U_s=220V, f=50Hz, R_s=3\Omega, L_s=6\times 10^{-6}H$
Load	$R_1=25\Omega, L_1=7\times 10^{-3}H$
APF parameters	$r=0.0001\Omega, L=5\times 10^{-3}H$
Switching frequency	$f=20kHz$
Other parameters	$U_{dc}^*=700V, C=5.5\times 10^{-4}F$

Using the resistor R_1 and inductor L_1 series equivalent nonlinear load, the controller parameters are optimized via IRSA with the following results: $k_1=9.293305$, $k_2=265.9742$, $k_3=38.5341$, $\alpha=0.485234$, $\varepsilon=420.2576$, $\sigma=0.8049327$, $\nu=0.8499738$, and $\varphi=0.2419748$. Then, taking phase-b as an example, the spectrum of the grid-side current shown in Fig. 6 presents the changes observed before and after the filter is added.

From the Figs. 6 and 7, it can be seen that the APF implementing the IRSA-FOCTSMC strategy initiates operation precisely at $t=0.04$ s, as indicated by the initial compensation current injection. Post-activation, the grid-side current waveform exhibits progressive harmonic suppression, achieving substantial waveform smoothing by $t=0.07$ s. Notably, the reference and compensation current trajectories show excellent convergence with near-perfect overlap beyond 0.07 s, confirming the controller's rapid dynamic response and precise tracking capability.

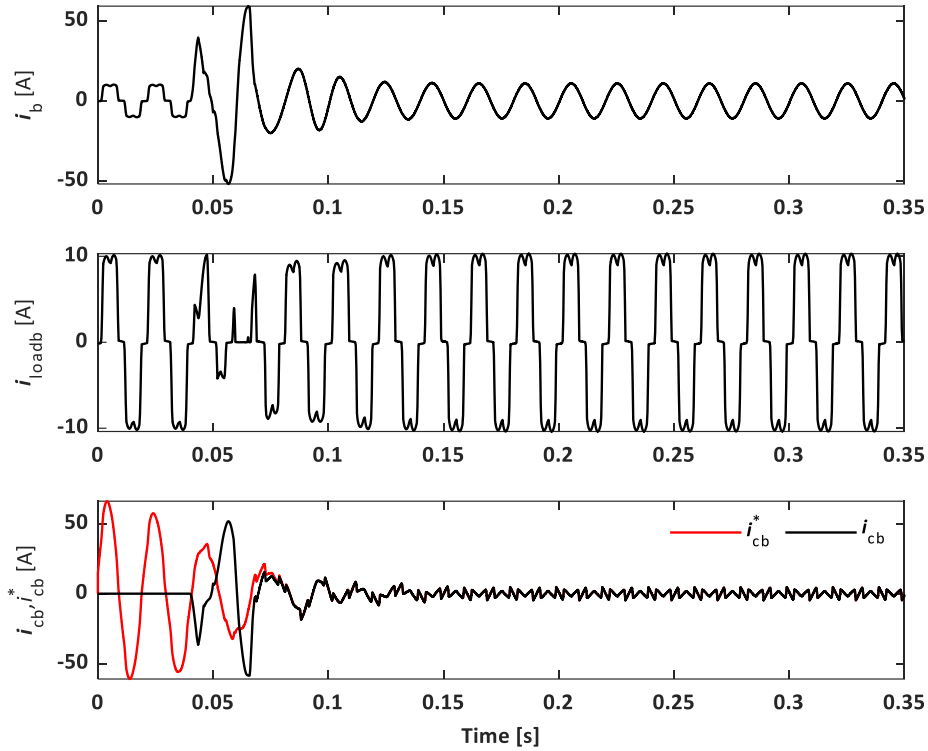


Fig. 6. Dynamic response diagram of IRSA-FOCTSMC.

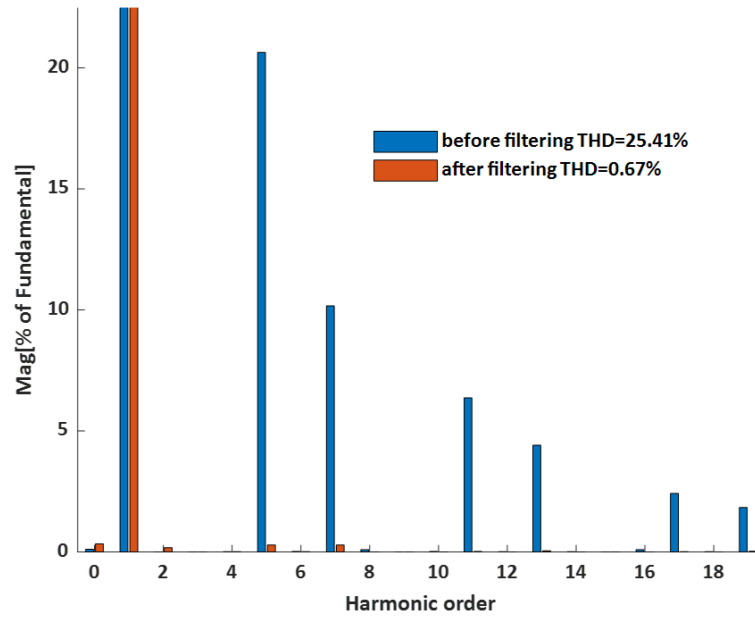


Fig. 7. Current spectrum on the grid side after filtering.

Fast Fourier Transform (FFT) analysis reveals the grid current's total harmonic distortion (THD) is reduced from 24.51% (pre-compensation) to 0.67% (post-compensation). This resultant 0.67% THD not only satisfies the most stringent IEEE 519-2022 requirement (<5%) but also exceeds premium power quality standards (<2%) for sensitive loads, demonstrating the effectiveness of the optimized control strategy.

To investigate the influence of the fractional order α on the filtering performance of the APF, three distinct values ($\alpha=0.25, 0.5$, and 0.75) are tested. The corresponding phase-b current response characteristics and their FFT spectra are then obtained and analyzed.

As clearly observed in Figs. 8-10, after implementing the APF while maintaining identical control parameters, the time required for the phase-b current waveform to transition from a distorted state to a smooth sinusoidal waveform is measured to be 0.06s, 0.04s, and 0.12s for fractional order α values of 0.25, 0.5, and 0.75, respectively. Furthermore, FFT analysis of the steady-state phase-b current revealed corresponding THD values of 1.03%, 0.7%, and 3.46% for these cases. These results demonstrate that the fractional order α significantly affects the harmonic suppression performance of the APF.

To further illustrate the merits of the proposed method, a comparison is made among the IRSA-FOCTSMC (namely, the proposed control method), the TSMC, the CSMC, the CTSMC, and the RSA-FOCTSMC. The absolute error and filtering effect of a-phase current tracking are obtained by constructing the corresponding simulation models and performing simulations, as shown in Table 3.

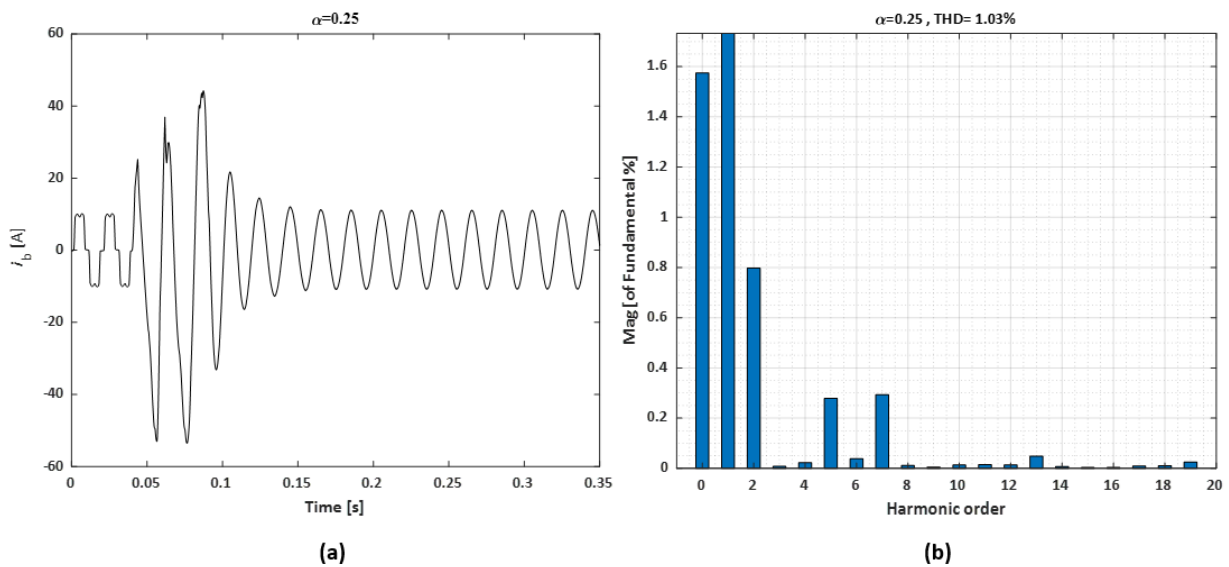


Fig. 8. Time-domain response and FFT spectrum for order $\alpha=0.25$: a) phase-b current response diagram; b) FFT analysis of phase-b current THD.

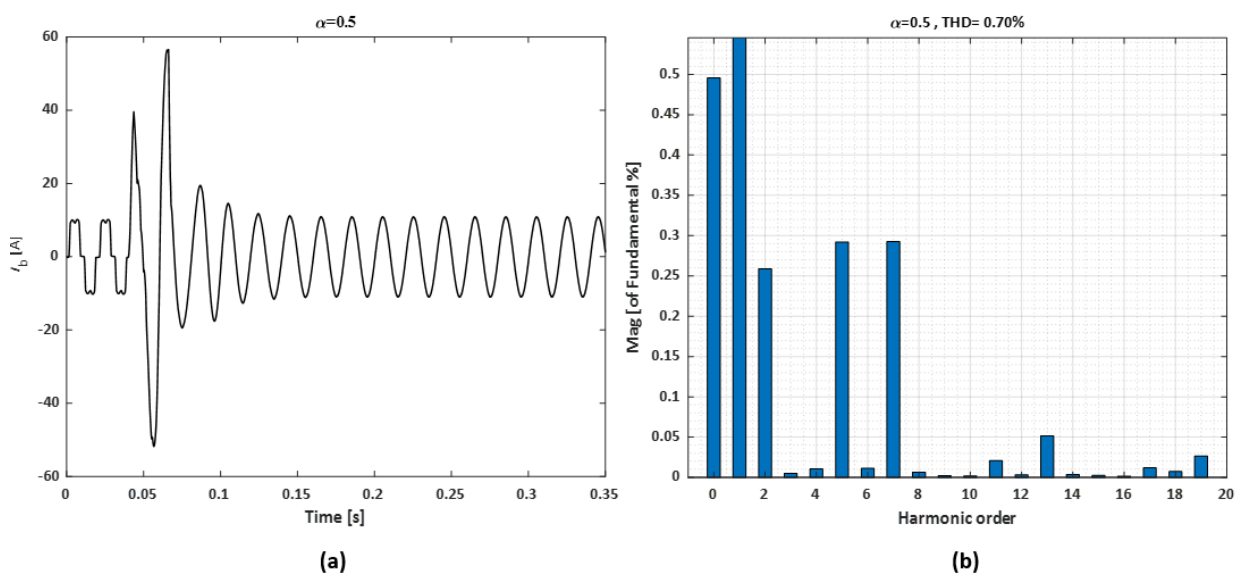


Fig. 9. Time-domain response and FFT spectrum for order $\alpha=0.5$: a) phase-b current response diagram; b) FFT analysis of phase-b current THD.

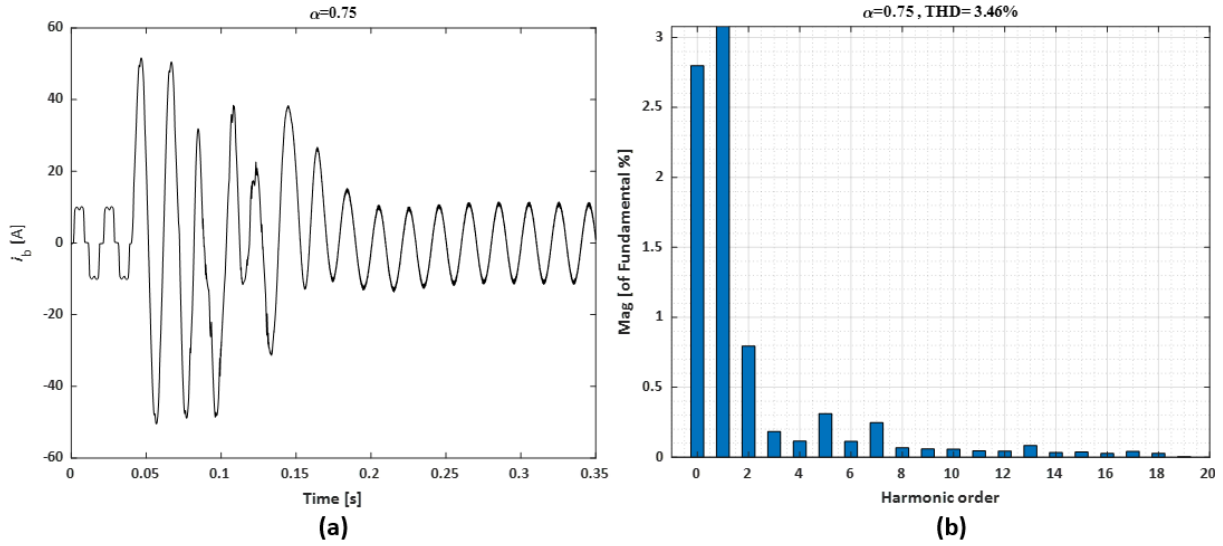


Fig. 10. Time-domain response and FFT spectrum for order $\alpha=0.75$: a) phase-b current response diagram; b) FFT analysis of phase-b current THD.

Table 3. Comparison of filtering effect under different control methods.

Control method	TSMC	CSMC	CTSMC	RSA-FOCTSMC	IRSA-FOCTSMC
THD/[%]	1.75%	1.40%	1.11%	1.01%	0.67%

From Table 3, it can be observed that the current THD value of the APF under the optimization control strategy proposed in this paper is lower than that of the other four optimization control strategies. This indicates that the proposed optimization control strategy can further improve the filtering performance of the APF.

In order to verify the robust performance of the controller designed in this paper, two distinct perturbations are simultaneously applied during simulation. For one, an internal parameter perturbation defined as $d(t)=1+0.1\sin(50\pi t)+0.4\cos(10\pi t)$ is introduced into the control system. For another one, a dynamic load with same resistance value is connected to the original load at $t=0.2s$ and the load is removed at $t=0.3s$. Finally, the resulting current tracking errors of the five control strategies under the combined perturbations are comparatively presented in Fig. 11.

As can be clearly seen from Fig. 11, when the external load is suddenly added and removed, the optimization control strategy proposed in this paper can minimize the fluctuation amplitude of the current tracking error of the APF. This demonstrates that the optimization control strategy proposed in this paper has better current tracking performance under the perturbations. Hence, more robustness is owned.

In order to rigorously assess the robustness performance of the proposed control scheme, three representative disturbance scenarios are systematically introduced in the simulation. Firstly, harmonic components are injected into the grid voltage, with the resulting waveform illustrated in Fig. 12. Secondly, an internal parameter perturbation is introduced in the controller, mathematically expressed as $d(t)=1+0.1\sin(50\pi t)+0.4\cos(10\pi t)$.

Thirdly, two same impedance dynamic loads are incorporated: the first load is activated at $t=0.2s$, followed by the second at $t=0.3s$, with both loads being simultaneously disconnected at $t=0.4s$. Finally, the current tracking performance and errors of five control strategies are comparatively analyzed under disturbance conditions, as shown in Figs. 13 and 14.

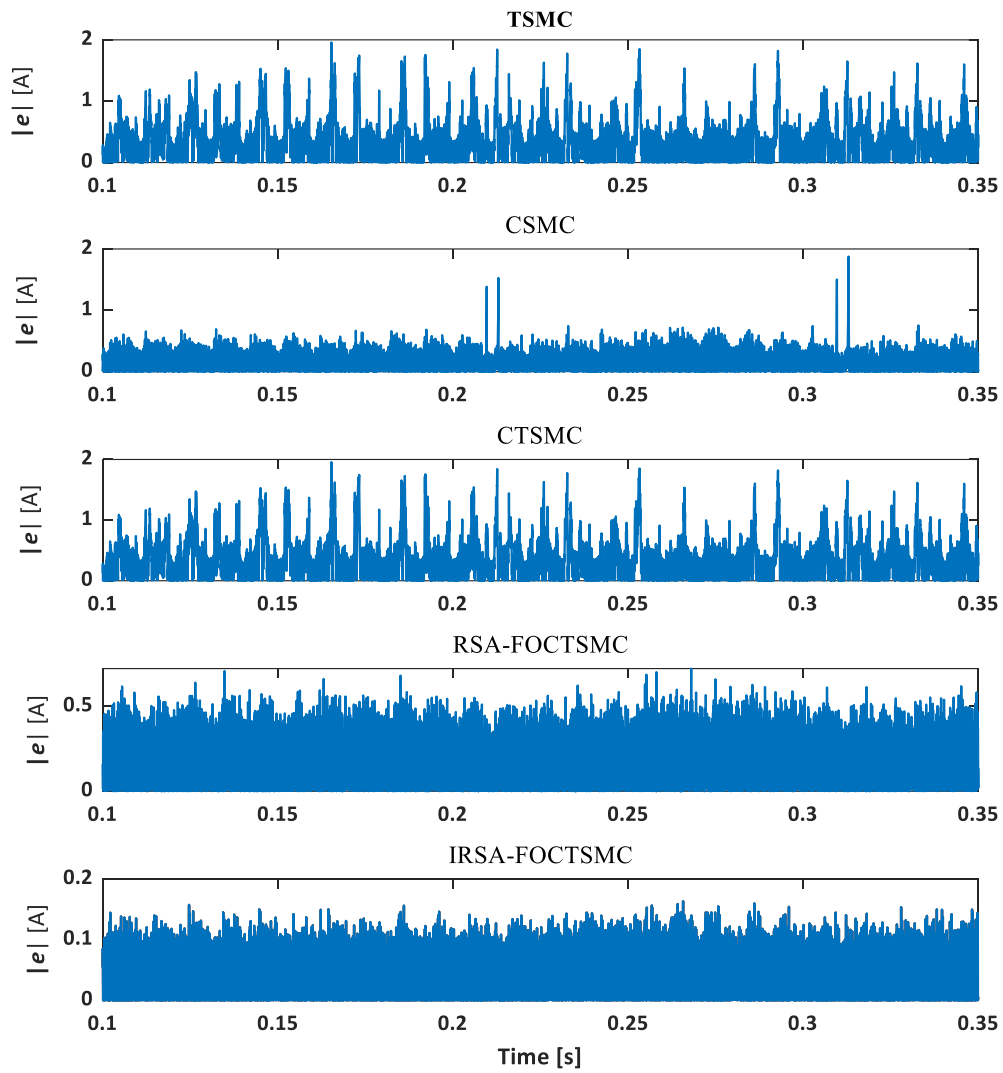


Fig. 11. Current tracking error diagram under two perturbations.

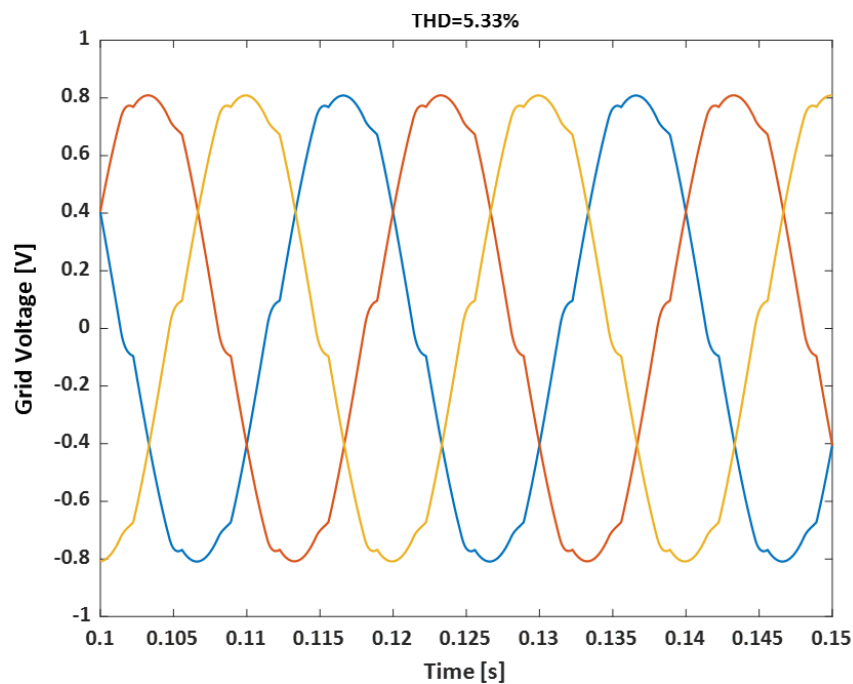


Fig. 12. Current tracking error diagram under two perturbations.

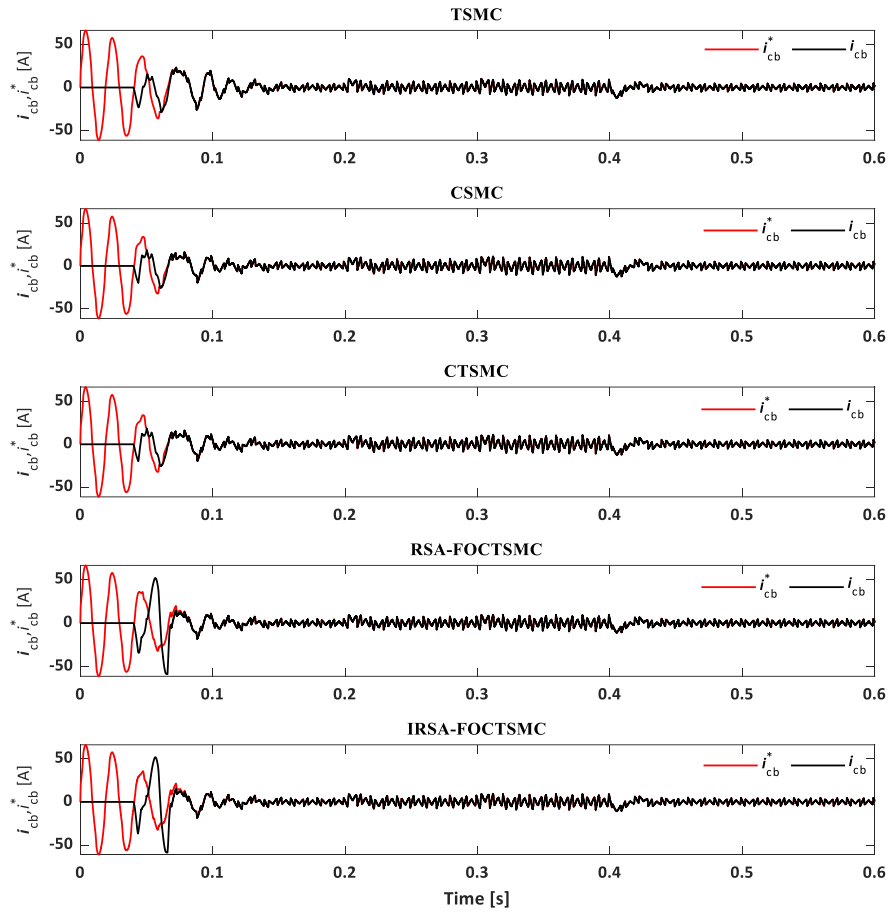


Fig. 13. Current tracking performance comparison among the five control strategies.

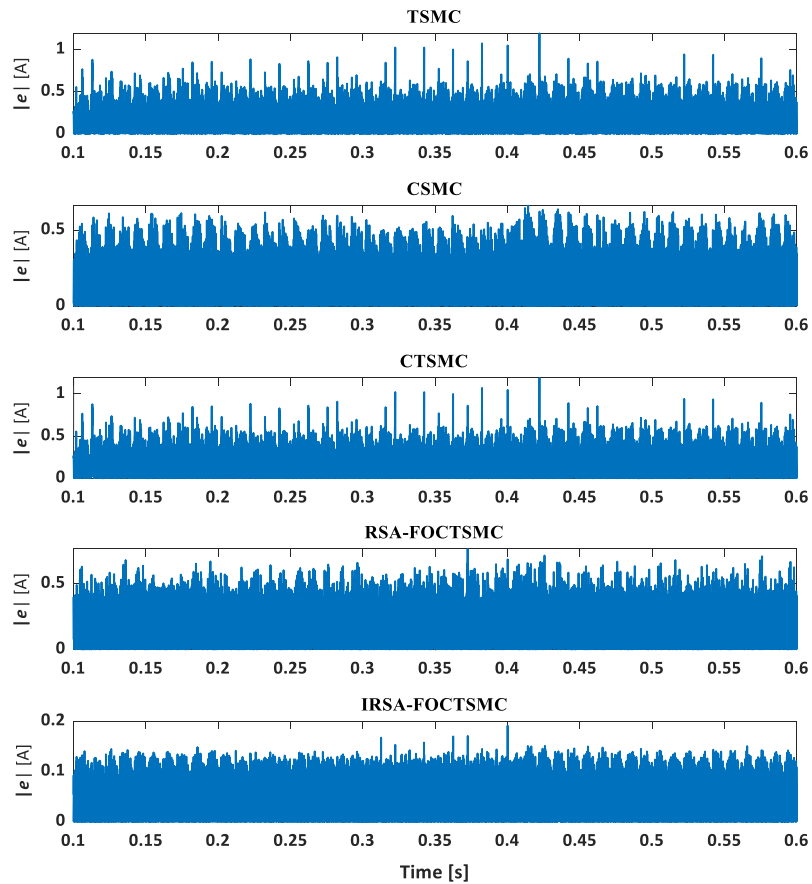


Fig. 14. Current tracking error diagram under three perturbations.

As shown in Figs. 13 and 14, all five control strategies maintain competent current tracking performance under multiple combined disturbances. Fig. 14 specifically presents the current tracking errors obtained through differential analysis. Notably, the proposed IRSA-FOCTSMC controller achieves a tracking error below 0.2A, outperforming other strategies with significantly smaller deviations. Moreover, the IRSA algorithm contributes to improved tracking accuracy. These findings collectively validate the strong robustness of the proposed control scheme.

5. DISCUSSION

The APF designed in this study can be effectively applied to rural distribution networks and distributed renewable energy (e.g., photovoltaic and wind power) grid-connected scenarios. In rural power grids, due to high line impedance, dispersed loads, and a significant proportion of nonlinear devices, harmonic pollution is prominent, leading to issues like voltage distortion and equipment overheating. By deploying APF at critical grid-connection points, harmonic currents can be compensated in real time, keeping the THD below 5% (referencing the IEEE 519-2022 standard), thereby significantly improving power quality.

Furthermore, the intermittent grid connection of distributed renewable energy sources introduces high-frequency harmonics, which are difficult for traditional passive filters to dynamically adapt to. The proposed APF, based on IRSA-FOCTSMC, can rapidly track harmonic variations, maintaining stable compensation performance even under fluctuating solar irradiance or wind turbine start-stop conditions. In practical deployment, considering the topological characteristics of rural grids, APF can be centrally installed at the low-voltage side of transformers or clustered distributed energy access points, achieving regional harmonic mitigation at a lower cost and avoiding the economic burden of household-by-household retrofitting.

However, the implementation of APF systems in rural distribution networks faces several technical and economic challenges: (1) grid impedance uncertainty due to inaccurate line parameters may degrade compensation accuracy, requiring robust online impedance identification algorithms; (2) the time-varying harmonic spectrum caused by high-penetration renewable energy integration necessitates advanced wideband control capability in APF design; and (3) economic constraints demand careful optimization between APF capacity allocation and grid infrastructure upgrade costs, where shared community-level APF deployment strategies may offer a cost-effective solution.

6. CONCLUSIONS

In this paper, the problem of harmonic management effectiveness of the APF is investigated, and a harmonic suppression method with the fractional-order complementary terminal sliding mode control strategy is proposed, and the parameters of the controller are optimized using the IRSA optimization algorithm. Then, it is compared with TSMC, CSMC, CTSMC and RSA-FOCTSMC on filtering effects and current tracking errors. The obtained results show that the optimized control algorithm - proposed in this paper - makes the harmonic management of the APF more effective and the current tracking error smaller.

The subsequent research will advance the current study through two key directions:

- a) Developing a multi-objective IRSA variant capable of concurrently optimizing THD, switching losses, and computational load to address inherent trade-offs in power quality control, with experimental validation of its performance.
- b) Implementation of adaptive robustness enhancement mechanisms specifically designed for weak grid conditions, featuring real-time impedance identification and dynamic gain scheduling. An experimental testbed will be established to verify this mechanism.

Acknowledgement: The presented investigation is supported by Yunnan Power Grid Technology Project under Grant YNKJXM20230455.

REFERENCES

- [1] C. Gong, Z. Cheng, W. Sou, C. Lam, M. Chow, "Collaborative distributed optimal control of pure and hybrid active power filters in active distribution network," *IEEE Transactions on Power Delivery*, vol. 38, no. 4, pp. 2326-2337, 2023, doi: 10.1109/TPWRD.2023.3240462.
- [2] P. Sarafrazi, S. Taher, A. Akhavan, "Robust backstepping controller based on nonlinear observer for shunt active filters to improve power quality in four-wire distribution systems," *Jordan Journal of Electrical Engineering*, vol. 10, no. 4, pp. 520-540, 2024, doi: 10.5455/jjee.204-1700421844.
- [3] J. Fei, Y. Chen, "Dynamic terminal sliding-mode control for single-phase active power filter using new feedback recurrent neural network," *IEEE Transactions on Power Electronics*, vol. 35, no. 9, pp. 9904-9922, 2020, doi: 10.1109/TPEL.2020.2974470.
- [4] K. Rai, N. Kumar, A. Singh, "Three-phase grid connected shunt active power filter based on adaptive q-lmf control technique," *IEEE Transactions on Power Electronics*, vol. 39, no. 8, pp. 10216-10225, 2024, doi: 10.1109/TPEL.2024.3398369.
- [5] W. Qi, X. Gao, C. Ahn, J. Cao, J. Cheng, "Fuzzy integral sliding-mode control for nonlinear semi-markovian switching systems with application," *IEEE Transactions on Systems, Man, and Cybernetics: Systems*, vol. 52, no. 3, pp. 1674-1683, 2022, doi: 10.1109/TSMC.2020.3034484.
- [6] H. Feng, Q. Song, S. Ma, "A new adaptive sliding mode controller based on the RBF neural network for an electro-hydraulic servo system," *ISA Transactions*, vol. 129, no. A, pp. 472-484, 2022, doi: 10.1016/j.isatra.2021.12.044.
- [7] Y. Liu, S. Laghrouche, D. Depernet, A. Djerdir, M. Cirrincione, "Disturbance-observer-based complementary sliding-mode speed control for pmsm drives: a super-twisting sliding-mode observer-based approach," *IEEE Journal of Emerging and Selected Topics in Power Electronics*, vol. 9, no. 5, pp. 5416-5428, 2021, doi: 10.1109/JESTPE.2020.3032103.
- [8] J. Fei, L. Liu, Y. Chen, "Finite-time disturbance observer of active power filter with dynamic terminal sliding mode controller," *IEEE Journal of Emerging and Selected Topics in Power Electronics*, vol. 11, no. 2, pp. 1604-1615, 2023, doi: 10.1109/JESTPE.2022.3222002.
- [9] Z. Bingul, O. Karahan, "A novel performance criterion approach to optimum design of PID controller using cuckoo search algorithm for AVR system," *Journal of the Franklin Institute*, vol. 355, no. 13, pp. 5534-5559, 2018, doi: 10.1016/j.jfranklin.2018.05.056.
- [10] M. Zhang, C. Xu, L. Li, Z. Wang, X. Zong, "Optimization of PID controller for stepper motor speed control system based on improved sparrow search algorithm," *Proceedings of the Institution of Mechanical Engineers, Part C: Journal of Mechanical Engineering Science*, 2024, doi: doi.org/10.1177/09544062241261268.
- [11] Z. Yu, Y. Sun, X. Dai, "Study on stability for interconnected uncertain fractional-order systems based on vector-bounded technique," *IEEE Transactions on Circuits and Systems II: Express Briefs*, vol. 71, no. 2, pp. 667-671, 2024, doi: 10.1109/TCSII.2022.3231710.
- [12] Z. Kang, H. Yu, C. Li, "Variable-parameter double-power reaching law sliding mode control method," *Automatika*, vol. 61, no. 3, pp. 345-351, May. 2020, doi: 10.1080/00051144.2020.1757965.

- [13] Q. Zhu, D. Huang, B. Yu, "An improved method combined SMC and MLESO for impedance control of legged robots' electro-hydraulic servo system," *ISA Transactions*, vol. 130, no 3, pp. 598-609, 2022, doi: 10.1016/j.isatra.2022.03.009.
- [14] L. Abualigah, M. Elaziz, P. Sumari, Zong W. Geem, A. Gandomi. "Reptile search algorithm (RSA): a nature-inspired meta-heuristic optimizer," *Expert Systems with Applications*, vol. 191, no. 15, pp. 116-158, 2022, doi: 10.1016/j.eswa.2021.116158.